GEOPHYSICS

# Structural response of α-quartz under plate-impact shock compression

**Sally June Tracy[1,2]*, Stefan J. Turneaure[3], Thomas S. Duffy[1]**



**Because of its far-reaching applications in geophysics and materials science, quartz has been one of the most extensively examined materials under dynamic compression. Despite 50 years of active research, questions remain concerning the structure and transformation of $SiO_2$ under shock compression. Continuum gas-gun studies have established that under shock loading quartz transforms through an assumed mixed-phase region to a dense high-pressure phase. While it has often been assumed that this high-pressure phase corresponds to the stishovite structure observed in static experiments, there have been no crystal structure data confirming this. In this study, we use gas-gun shock compression coupled with in situ synchrotron x-ray diffraction to interrogate the crystal structure of shock-compressed α-quartz up to 65 GPa. Our results reveal that α-quartz undergoes a phase transformation to a disordered metastable phase as opposed to crystalline stishovite or an amorphous structure, challenging long-standing assumptions about the dynamic response of this fundamental material.**

## INTRODUCTION

Laboratory shock wave experiments have long played an important role in characterizing properties of geophysical materials at the high pressure and temperature conditions of the deep Earth (*1*). Shock-compression experiments yield pressure-temperature states comparable to planetary adiabats, thus requiring minimal extrapolation for geophysical application. Moreover, shock loading presents a unique capability to study impact phenomena in real time, providing insight into natural impact processes relevant to planetary formation and evolution. Quartz ($SiO_2$) is one of the most abundant minerals of Earth's crust and is widely distributed in different rock types. As a result, characterizing the dynamic response of $SiO_2$ is important for interpretation of shock metamorphism in samples from terrestrial impact sites (*2*, *3*). Furthermore, quartz serves as an archetype for the silicate minerals of the crust and mantle. Hence, characterizing the high-pressure, high-temperature behavior of quartz is important for understanding potential silica-rich regions of the deep Earth.

The high-pressure behavior of quartz has been the subject of extensive experimental studies. At ambient conditions, the stable polymorph of $SiO_2$ is the trigonal α-quartz structure ($P3_221$), composed of a corner-linked framework of $SiO_4$ tetrahedra. On the basis of the equilibrium phase diagram, $SiO_2$ adopts a series of crystalline phases under pressure from quartz to coesite ($C2/c$) to stishovite (rutile structure, $P4_2/mnm$) to a $CaCl_2$-type phase ($Pnnm$) (*4*). In addition, a number of metastable forms of $SiO_2$ have been observed experimentally or predicted theoretically (*5*–*10*). Because of the high kinetic barriers associated with these transitions, when compressed in a diamond anvil cell at 300 K, quartz persists to above 20 GPa, where it transforms to a disordered, dense metastable phase (*7*, *11*).

The behavior of quartz under shock compression differs markedly from its static response. The Hugoniot (Fig. 1) is characterized by a highly compressible region often called the "mixed-phase region" that initiates at ~15 GPa and reaches completion at ~40 GPa, at which point the material compressibility decreases appreciably. On the basis of Hugoniot data and thermodynamic considerations, it is often assumed that the high-pressure phase on the quartz Hugoniot corresponds to crystalline stishovite (*12*–*14*). However, there is no direct evidence demonstrating this, and the structure of the high-pressure phase remains a subject of continued debate.

The sequence of phase transitions occurring in dynamically compressed quartz and the role of kinetics remain unknown. For α-quartz shocked between 30 and 65 GPa, calculated Hugoniot temperatures range from ~1500 to 4000 K (*15*). Recovery experiments and samples collected at natural impact sites are found to consist primarily of amorphous material with trace quantities of stishovite (*3*). Because of the high-temperature release path, it is an open question whether amorphization occurs during compression

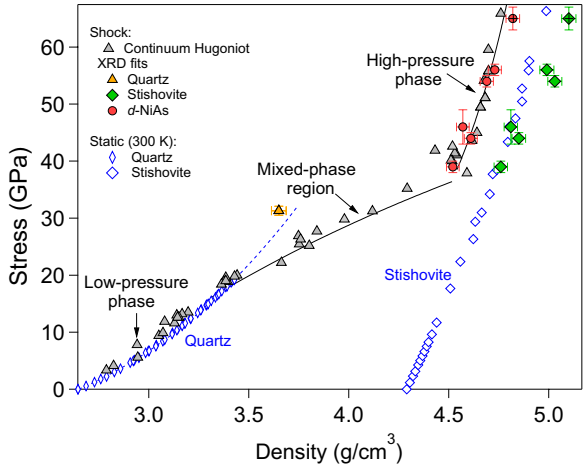


**Fig. 1. Shock Hugoniot curve for quartz.** Continuum Hugoniot data are shown as gray triangles (*31*–*34*). Black curves are guides to the eye. Blue open symbols are the 300-K static compression data for stishovite (*35*) and α-quartz (*22*). Blue dashed line is an extrapolated equation of state fit to the 300-K quartz data. Densities derived from Le Bail fits to the Z-cut quartz XRD data using α-quartz, stishovite, or *d*-NiAs structures are shown as solid orange, green, and red symbols, respectively. X-ray fits to the off-Hugoniot double-shock state at 65 GPa are indicated with crosses.

[1]Department of Geosciences, Princeton University, Princeton, NJ 08544, USA. [2]Geophysical Laboratory, Carnegie Institution for Science, Washington, DC 20015, USA. [3]Institute for Shock Physics, Washington State University, Pullman, WA 99164, USA. *Corresponding author. Email: sjtracy@carnegiescience.edu

or release. On more general grounds, it has been suggested that reconstructive transformations involving tetrahedral to octahedral coordination changes are kinetically limited on shock wave time scales, and hence, there is insufficient time for the formation of stishovite in a laboratory shock wave experiment (*16*). Accordingly, it has been contended that the high-pressure phase of quartz instead corresponds to a metastable intermediate or a dense amorphous structure (*17*, *18*). Using traditional continuum diagnostics, the crystal structure of high-pressure phases that form under dynamic compression cannot be determined experimentally. As a result, key questions concerning the nature of the mixed-phase region and the structure of the high-pressure phase(s) on the quartz Hugoniot remain unresolved.

Recently, in situ x-ray diffraction (XRD) measurements under gas-gun loading have shown that fused silica remains amorphous under shock compression until 35 GPa, and for higher stresses, it transforms to polycrystalline stishovite (*19*). Stishovite formation has also been observed in laser-shock experiments in fused silica (*20*) and in recovery experiments on porous sandstone (*21*). Here, we use time-resolved XRD measurements coupled with gun-based dynamic compression to probe the crystal structure of α-quartz under shock compression. Plate-impact loading provides a uniform, well-defined state of uniaxial strain within the shocked quartz. The XRD data provide a complete picture of the material response by revealing new details of the crystal structure for stresses from 31 to 65 GPa.

## RESULTS

Figure 2 shows representative two-dimensional (2D) XRD images from Z-cut quartz shots at 31 and ~63 GPa. For the lower-stress experiment, peaks corresponding to compressed α-quartz can be identified. In the 2D image, the compressed peaks appear as localized bright spots much broader than the ambient single-crystal Laue spots, indicating that the shocked Z-cut quartz developed a mosaic spread of several degrees. On the basis of peak fitting the intense (101) α-quartz peak, the density of the compressed α-quartz can be estimated to be ~3.65 g/cm$^3$. This density is consistent with an extrapolation of the 300-K equation of state of α-quartz from static compression experiments (*22*), where the modest offset is consistent with the higher temperature along the Hugoniot (Fig. 1). In addition to the α-quartz peaks, there are a number of other peaks that cannot be assigned to the α-quartz structure, indicating that the material has partially undergone a pressure-induced phase transformation. The coexistence of low- and high-pressure phases indicates that the Hugoniot state is a mixed-phase region near 30 GPa. The scattering from the transformed material has more extended arcs, albeit with pronounced azimuthal intensity variations. This finding indicates that preferred orientation (or texture) persists above the phase transformation.

At ~63 GPa (Fig. 2B), the α-quartz peaks have disappeared, indicating a complete transformation to a high-pressure phase. For the higher angle peaks, the width of the profiles indicates modest broadening on top of the expected instrumental contribution. These results demonstrate that quartz transforms to a high-pressure phase with crystalline order, and show that the high-pressure phase is not amorphous as had been proposed in the literature (*17*, *18*).

Figure 3 shows a series of azimuthally integrated diffraction patterns for Z-cut quartz obtained for stress states ranging from

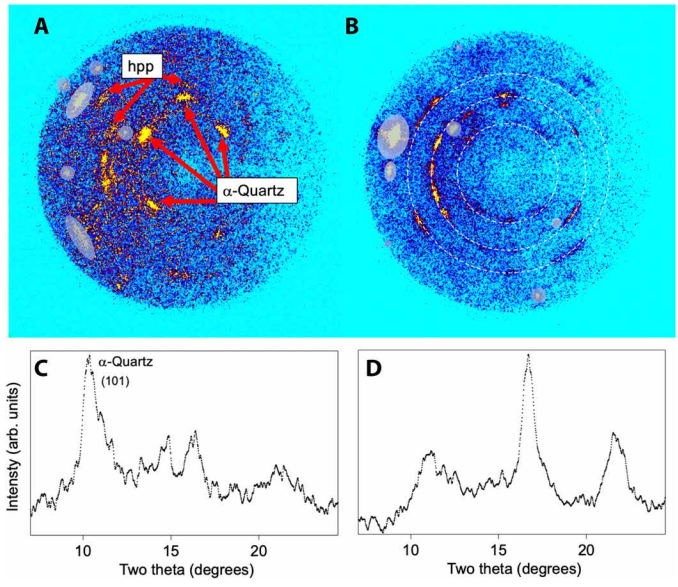


**Fig. 2. 2D XRD images and corresponding integrated XRD patterns.** (**A**) 2D XRD image for Z-cut quartz shock-compressed to 31 GPa (shot 16-5-033, frame 3). Diffraction is observed from both compressed α-quartz and a high-pressure phase (hpp), indicating that the material has been shocked into a mixed-phase region. (**B**) 2D XRD image taken for Z-cut quartz shock-compressed to ~63 GPa (shot 16-5-118, frame 3). This frame was captured after partial reshock from the LiF window and constitutes a combination of $SiO_2$ reshocked to 67 GPa and material in the initial 58-GPa single-shock state. Dashed lines indicate three strong reflections seen in the integrated pattern (below). Gray regions in (A) and (B) are diffraction from the LiF impactor, the LiF window, or Laue spots from the uncompressed or elastically compressed α-quartz; these regions were masked during azimuthal integration. Because of the diffraction geometry (fig. S4A), scattered x-rays recorded on the right half of the detector undergo higher attenuation due to greater sample absorption. (**C**) Integrated XRD pattern corresponding to the 2D image shown above. The peak around ~14° is consistent with the LiF (200) peak. (**D**) Integrated XRD pattern corresponding to the 2D image shown above.

31 to 65 GPa. Other than the XRD profile collected at 65 GPa, all measured XRD profiles shown in Fig. 3 are from frames captured before the shock wave has traversed the entire thickness of the Z-cut quartz sample and correspond to Hugoniot states. The pattern collected at 65 GPa corresponds to a double-shock state produced by reshock from 56 to 65 GPa at the lithium fluoride (LiF) window. The shocked Z-cut quartz diffraction data collected for Hugoniot stresses at 31 to 35 GPa exhibit an intense peak at ~10° 2θ, consistent with the compressed α-quartz (101) reflection. In addition, new diffraction peaks are observed at 16° and 21°. For shock stresses above 35 GPa, the α-quartz (101) peak can no longer be detected and the diffraction pattern contains a broad feature spanning 9° to 12° 2θ with distinctly sharper peaks near 16° and 21°. These two new peaks are from discrete regions around the diffraction rings (see Fig. 2), indicating significant texture both in the mixed-phase region and in the high-pressure region.

Figure 4 shows a comparison of diffraction data from shocked X-cut, Y-cut, and Z-cut quartz collected at 56 to 65 GPa. Similar to the Z-cut quartz results, the diffraction patterns for X-cut and Y-cut quartz also indicate significant texture of the high-pressure phase, as evidenced by localized scattering as opposed to extended Debye Scherrer rings. While the azimuthal intensity variations of

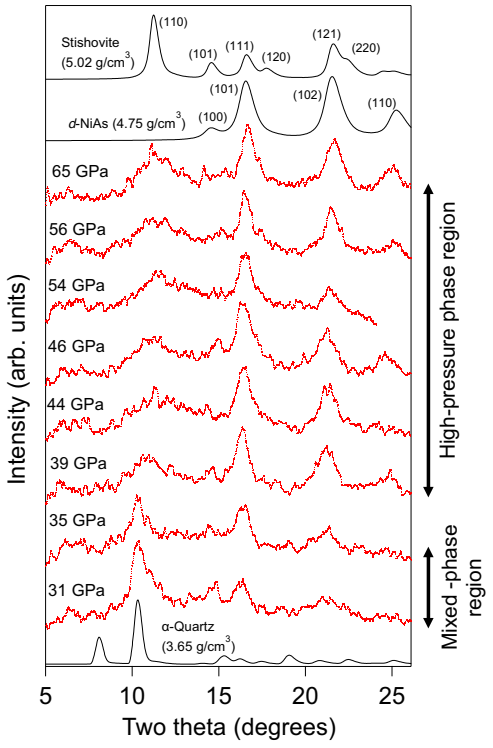


**Fig. 3. Azimuthally integrated XRD patterns.** XRD patterns collected for a series of plate-impact experiments for Z-cut quartz starting material with peak stress states between 31 and 65 GPa. Shot numbers and x-ray frame times relative to shock breakout at the rear surface of the quartz are listed in table S5. Note that the 54-GPa shot was collected during an experiment with a longer sample-detector distance, leading to a lower angle cutoff in the data. Simulated diffraction patterns (accounting for the spectral shape of the pink x-ray beam) are shown for compressed α-quartz (3.65 g/cm$^3$) as well as both stishovite (5.02 g/cm$^3$) and the defective niccolite structure (4.75 g/cm$^3$). The simulated patterns shown use lattice parameters based on fits to data for α-quartz in the mixed-phase region and for the stishovite and defective niccolite structures in the high-pressure region.

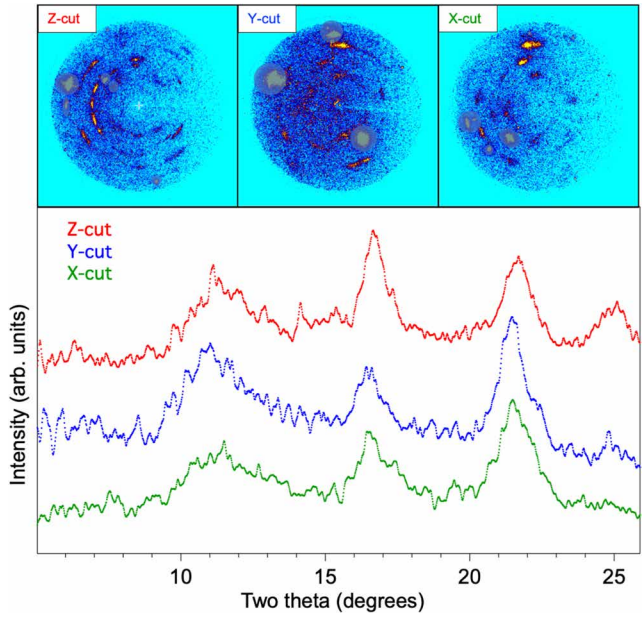


**Fig. 4. XRD data for single-crystal quartz shock-loaded to 56 to 65 GPa along different crystallographic axes.** Data for Z-cut (shot 16-5-022, frame 3) and Y-cut (shot 16-5-119, frame 3) samples were collected during double-shock experiments at 65- and 64-GPa final stress, respectively. Data for X-cut quartz (shot 16-5-126, frame 2) were collected while the initial shock wave was propagating through the sample, bringing the material to 56-GPa shock stress. 2D images are shown at the top with LiF and uncompressed quartz spots masked, and integrated patterns are shown at the bottom.

the diffraction patterns are different for different orientations, the integrated patterns indicate that all orientations transform to the same phase under shock compression.

Figure 5 compares the diffraction data for shocked polycrystalline novaculite (natural microcrystalline quartz) with the diffraction patterns collected for Z-cut quartz and fused silica shocked to similar peak stresses (63 to 66 GPa). In previous experiments at the Dynamic Compression Sector (DCS), we used in situ XRD coupled with gun-based shock compression to examine the structure of shocked fused silica (*19*). That study demonstrated that silica glass adopts a dense amorphous structure for shock pressures up to 35 GPa, above which it transforms to nanocrystalline stishovite. A comparison of the stishovite diffraction pattern obtained from fused silica starting material to the diffraction patterns for the α-quartz starting materials shows that while the integrated diffraction patterns for single-crystal and polycrystalline quartz have similarities, they are distinct from the stishovite pattern observed for shocked fused silica.

The three shots in Fig. 5 all correspond to double-shock measurements, where XRD data were collected after the shock waves propagated through the $SiO_2$ sample reflecting from the LiF window as a reshock, resulting in a uniform final stress state. Diffraction data for polycrystalline novaculite samples shocked to lower peak stresses show similar features (fig. S7). In the polycrystalline data, the strong peak at 9.5° corresponds to a residual ghost peak from the ambient strong (101) α-quartz reflection. This peak is the result of incomplete decay of the phosphor scintillator detector between successive x-ray frames and does not arise from scattering from the compressed sample. The signal intensity is notably lower for the polycrystalline data compared to the single-crystal data, yielding lower signal to noise. While the integrated diffraction pattern is similar to single-crystal data, the diffraction rings are smooth and continuous without the azimuthal intensity variations from preferred orientation observed in the single-crystal data.

## DISCUSSION

A comparison of the diffraction patterns for the high-pressure phases of silica glass and α-quartz (Fig. 5) at similar shock pressures highlights the clear distinction in the structure of the high-pressure phase depending on the starting material. Here, we reveal two key distinctions in the structure of α-quartz under shock loading compared with fused silica: (i) As opposed to the densification observed below 35 GPa for silica glass, the region below ~40 GPa on the α-quartz Hugoniot represents a crystalline mixed-phase region, that is, a coexistence of compressed α-quartz and transformed high-pressure material; (ii) while α-quartz undergoes a phase transformation to a crystalline phase at a similar shock pressure as silica glass, the structure of the high-pressure phase bears similarity to the

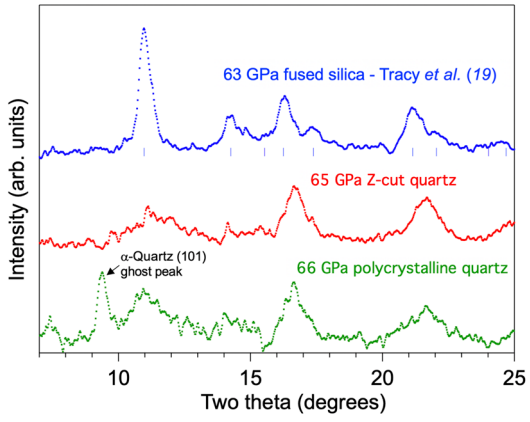


**Fig. 5. Comparison of XRD data collected for different starting $SiO_2$ materials after shock compression.** Starting materials are fused silica [from experiment 17-5-037 in (*19*)], Z-cut α-quartz (experiment 16-5-022, frame 3), and a polycrystalline natural α-quartz sample (experiment 17-5-011, frame 3). Expected stishovite peak locations are shown as blue ticks below the fused silica pattern. All patterns correspond to data collected after the initial shock wave reflects from the LiF window, reshocking the sample to final stresses between 63 and 66 GPa.

stishovite structure but is distinctly different. In particular, the diffraction pattern from α-quartz does not exhibit an intense low-angle peak corresponding to the stishovite (110) reflection.

The absence of the strong stishovite (110) peak is consistent across multiple orientations of single crystals (Fig. 4) as well as polycrystalline starting material (Fig. 5) and therefore cannot be attributed to residual texture due to an orientation relationship between the starting material and the high-pressure phase. While we do not observe a sharp low-angle peak in the XRD patterns, there is a broad, weaker feature peaked at $Q$~2.3 $Å^{-1}$ [$Q = 4\pi\sin(\theta)/\lambda$] that persists across the entire measured stress range (Fig. 3). One possible explanation is that this feature corresponds to partial amorphization of the sample (*16*–*18*, *23*). However, this feature exhibits some azimuthal intensity variations on the 2D diffraction image (Fig. 2B), inconsistent with scattering from an amorphous material. Furthermore, this low-angle feature occurs at lower $Q$ than the first sharp diffraction peak (FSDP) of $SiO_2$ glass observed in static compression experiments in this pressure range (see fig. S9) (*24*–*27*). This differs from shocked silica glass (*19*), where the FSDP overlaps static data. While the higher temperature of the Hugoniot states needs to be accounted for, recent results show that elevated temperatures can enable additional compression mechanisms, allowing the glass to achieve a denser state than it can at lower temperatures (*28*, *29*). In addition, the broad character and low intensity relative to other peaks remain fairly constant with increasing pressure, despite the large change in expected temperature over this range, which should promote crystallization.

The textured Debye-Scherrer rings of the high-pressure phase (Fig. 2) are in marked contrast with the results of recent molecular dynamics simulations for both α-quartz and silica glass (*30*). In these simulations, uniaxial loading induces picosecond amorphization of the α-quartz crystal structure, followed by nanosecond stishovite crystallization via homogeneous nucleation and growth. After amorphization, the simulations for α-quartz proceed via a transformation mechanism that mirrors that of silica glass under similar loading conditions. Unlike silica glass, where we observed smooth powder-like rings (*19*), the residual texture in our data is hard to reconcile with a nucleation and growth model. It is unlikely that within the time scale of our measurements (several hundred nanoseconds), the requisite grain growth could occur to yield this degree of texture. Instead, the orientation-dependent texture suggests a topotactic relationship between the α-quartz starting material and the high-pressure phase. Accordingly, it is likely that the transformation involves a displacive or shear-mediated mechanism preserving some degree of atomistic neighbor memories.

Figure 1 shows the Hugoniot for α-quartz in pressure-density space including selected previous continuum data (*31*–*34*). The 300-K static compression data for stishovite (*35*) along with the densities determined from fits to our XRD data in the high-pressure region are also shown. The solid green symbols in Fig. 1 show the densities determined from Le Bail fits to the entire diffraction line profile assuming the stishovite structure (see fig. S3). Details of the fits, including the accounting for the spectral shape of the pink x-ray beam, are described in the Supplementary Materials. X-ray densities derived from fits assuming the stishovite structure are denser than both the continuum Hugoniot and the 300-K isothermal data for stishovite. The high temperatures generated during shock loading require the Hugoniot to necessarily be offset to lower densities relative to the 300-K isotherm. Hence, the assignment of the high-pressure phase under shock loading to the stishovite structure can be ruled out.

Numerous metastable high-pressure polymorphs of $SiO_2$ have been reported from both theoretical calculations and static compression experiments (*5*–*10*, *36*–*38*). These structures can generally be described as various silicon cation fillings of the octahedral voids within an approximately hexagonal close-packed (hcp) oxygen lattice (*6*). A wide range of energetically competitive structures can be generated by modifying the silicon filling pattern and the degree of distortion of the oxygen sublattice. Within this context, stishovite can be described as a distorted hcp array of oxygen anions, where one-half of the available octahedral interstices are filled by silicon ions forming linear chains of edge-sharing $SiO_6$ octahedra. When transposed into the rutile unit cell, this silicon ordering represents a filling of every other void along the tetragonal <110> direction, yielding an intense (110) peak in the stishovite diffraction pattern. As a result, any disorder in the silicon sublattice causes destructive interference along this direction, effectively reducing the intensity of the (110) peak.

The defective niccolite structure (*d*-NiAs or $Fe_2N$-type) can be considered the most general structure within this family of $SiO_2$-oxygen close-packed phases. In this structure, the oxygen anions are arranged in an ideal hcp lattice and silicon cations are distributed randomly across the octahedral voids with an occupancy factor of $^1/_2$. This structure has been observed as a metastable phase in heated diamond anvil cell experiments for pressures between 30 and 60 GPa and temperatures between 900 and 1200 K (*8*, *37*, *39*). While the overwhelming majority of gas-gun shock recovery experiments on $SiO_2$ report finding quartz or amorphous material, there are two reports in which a very small amount of *d*-NiAs phase was identified together with quartz and glass (*36*, *40*). Figure **3** includes simulated diffraction patterns for both the *d*-NiAs and stishovite structures. While the patterns are generally similar, the stishovite pattern contains additional peaks that arise from coherent scattering from ordered planes of silicon within the structure. Notably, the *d*-NiAs pattern has no low-angle peak due to the lack of any long-range

silicon order. Furthermore, for structures of equivalent density, the stishovite peaks are offset to slightly lower angles. This shift arises from the lower packing efficiency of the distorted oxygen framework as opposed to the ideal hcp lattice of the *d*-NiAs structure. In addition to stishovite densities, Fig. **1** also includes densities derived from fits to the *d*-NiAs structure. In this case, the two prominent peaks in the diffraction patterns are indexed to the (101) and (102) peaks of the hexagonal *d*-NiAs unit cell as opposed to the (111) and (121) peaks of the tetragonal stishovite structure (Fig. **3**). In comparison to the unphysically high densities determined from the stishovite fits, Le Bail profile refinements assuming the *d*-NiAs structure yield densities that are consistent with the continuum Hugoniot data. Fits to the diffraction data for X- and Y-cut quartz starting materials as well as polycrystalline quartz yield an overall similar result (fig. S6). The densities in the mixed-phase region could not be accurately determined because of overlapping diffraction peaks for multiple phases.

While fits to the *d*-NiAs structure agree with the previous continuum pressure-volume Hugoniot results (*31*–*34*), this structure cannot account for the diffuse low-angle peak observed consistently across the high-pressure region (Fig. 3). It is possible to explain the XRD patterns in terms of the *d*-NiAs phase coexisting with some amount of dense amorphous material. In this case, the diffuse peak could be attributed to the retention of some amount of an amorphous metastable intermediate, consistent with molecular dynamics simulations (*30*), although the azimuthal intensity variation (Fig. 2B), as well as the discrepancy in the position of this feature compared to the FSDP from $SiO_2$ glass under static compression, complicates this interpretation.

A second explanation for the observed diffraction patterns in the high-pressure region is a structure composed of a hcp oxygen framework filled with silicon cations lacking well-defined long-range order. A comparison of diffraction patterns for the various metastable high-pressure polymorphs of $SiO_2$ reveals an overall similarity in the high scattering angle peaks but distinctions in the low-angle peak position(s) (fig. S8). These differences can be attributed primarily to various silicon ordering schemes within an hcp-like oxygen lattice. The diversity of metastable $SiO_2$ phases indicates a complex energy landscape with numerous competing structures of similar energy.

There is a large body of work exploring both the structural interrelationships and transformation mechanisms between low-pressure $SiO_2$ tetrahedral coordination structures and various high-pressure six-coordinated phases, both stable and metastable (*6*, *41*–*43*). Within this context, each structure is defined by an ordering of the silicon cations within the tetrahedral and octahedral voids in a quasi–close-packed oxygen framework. The pathways between structures can be broken down into sets of transformations involving some combinations of displacive and ordering mechanisms. In recent years, new studies have revisited this subject with various phenomenological approaches including excited-state transition pathway calculations and ab initio molecular dynamics (*9*, *10*, *30*). These simulations suggest that under nonhydrostatic conditions, the quasi–body-centered cubic oxygen sublattice that describes α-quartz can transform via a martensitic mechanism (Burgers path) to an hcp oxygen lattice (*9*, *38*). These calculations give credence to a model in which the oxygen scaffolding responds rapidly to compression via a diffusionless mechanism, followed by a slower reordering of the silicon cations within their newly formed environment.

Because of the fast time scales of dynamic compression experiments, it is likely that while the oxygen sublattice can respond readily to loading, the diffusive motion of the silicon cations is kinetically limited. A plausible model involves a shear-mediated transformation of the oxygen lattice to a quasi-hcp structure followed by a diffusion-limited reordering of silicon. Within the nanosecond time scale of shock wave experiments, kinetic barriers may prevent the silicon cations from finding the absolute energy minimum, and instead, local regions may minimize energy by adopting various arrangements. The diffraction pattern from this type of partially disordered structure would contain well-defined peaks associated with the oxygen lattice but lack the low-angle peak associated with fixed silicon order. As opposed to the fully disordered case represented by *d*-NiAs, there are local regions of short-range order, representing a distribution of periodicities centered about a *d*-spacing consistent with the observed low-angle peak. In this way, the structural transformation on the Hugoniot represents a metastable intermediate arising from a bimodal transformation yet to reach completion.

In addition to probing the structure under compression, the time resolution of our measurements allows us to probe the structural evolution of the sample on release. Targets without a window bonded to the $SiO_2$ will have a release wave propagate back into the sample when the shock wave reaches the free surface. While the temperature can remain high as the sample releases isentropically, pressure drops rapidly when rarefication waves from the sample free surface and/or edges of the target reach the sample center. Figure 6 shows the results of one such experiment in which a novaculite sample was shocked to 35 GPa. An XRD frame was recorded on compression, and two XRD frames were recorded between 200 and 600 ns after the onset of longitudinal stress release from the novaculite free surface. The impact velocity was chosen so that the peak Hugoniot pressure was below 40 GPa to avoid potentially crossing the liquidus during shock release based on the predicted isentropic release path (*15*).

In Fig. 6, the reemergence of a strong peak at 9° 2θ at late times is consistent with the ambient pressure α-quartz (101) diffraction peak. In addition, it appears that a portion of the sample is amorphized, evidenced by the broad feature peaked at ~8° to 9° 2θ. While it is possible that trace amounts of the high-pressure phase are retained on release, there is no evidence for this within the resolution

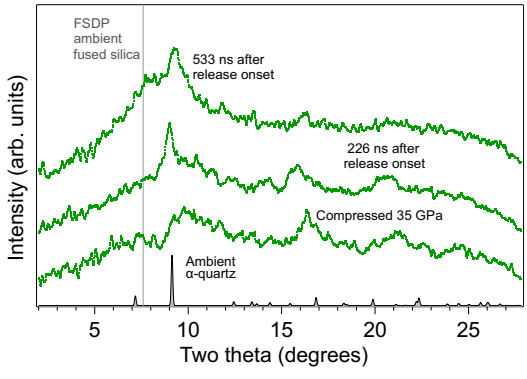


**Fig. 6. Integrated XRD patterns collected after release from a peak stress of 35 GPa for the novaculite starting material (experiment 17-5-019).** Compressed state data are from the second frame and have been background-subtracted to remove uncompressed α-quartz peaks from the material ahead of the shock front. Peak positions for ambient α-quartz are shown at the bottom, and the FSDP position for silica glass at ambient pressure is shown as a vertical gray line.

of our measurements. Scattering from the quenched glass is peaked at a distinctly higher $Q$ than the FSDP for ambient fused silica, while the α-quartz (101) peak indicates that pressure is fully released. Because of the overlap of the α-quartz (101) peak, amorphous scattering from the polycarbonate impactor, and amorphous scattering from the sample, it is challenging to assess the FSDP of the quenched glass with a high degree of accuracy. However, a comparison of the amorphous feature observed after release from the shocked state (~1.75 $Å^{-1}$) to the expected peak position for ambient silica glass (1.54 $Å^{-1}$) indicates that the released material is consistent with a densified glass. This is evidence that the material forms a densified (diaplectic) glass during rapid stress release from the shocked state. In shock recovery experiments for Hugoniot stresses between 25 and 50 GPa, recovered samples show primarily amorphous material ~5 to 10% denser than ambient silica glass. Above a threshold pressure, where the material is expected to melt on release, the recovered material corresponds to low-density glass with a structure similar to ambient fused silica. This result is consistent with both samples recovered from natural impact sites (*2*) and recent laser compression experiments that reported evidence for diaplectic glass formation in shock-compressed fused silica (*20*). In the present work, the sample undergoes a complex unloading history due to multiple wave interactions, and further experiments are needed to better constrain the released state.

XRD measurements provide direct crystallographic evidence of the phase transition from α-quartz to a disordered high-pressure crystalline phase under shock compression, challenging long-standing assumptions regarding the structure of shocked quartz (*12*–*14*). Upon shock compression to 31 to 35 GPa, our XRD results show evidence for compressed α-quartz in combination with new XRD peaks from transformed material, indicating that the material is being shocked into a mixed-phase state. For shock pressures from 39 to 65 GPa, quartz fully transforms to a new structure. The compressed α-quartz densities derived from fits to the XRD patterns in the mixed-phase region are consistent with an extrapolation of the 300-K equation of state of α-quartz from static compression experiments (*22*). The diffraction data from the transformed material are distinctly different from the stishovite pattern observed for shocked fused silica (*19*). The transformed phase exhibits a broadened low-angle peak arising from silicon site disorder within a close-packed oxygen framework. This structure can be described as a defective niccolite structure with considerable silicon short-range order. This result indicates that α-quartz transforms to a metastable high-pressure phase as opposed to crystalline stishovite, in contrast to the behavior of fused silica under shock loading. For single-crystal samples, a high degree of crystalline texture persists above the phase transformation, ruling out the amorphous intermediate proposed by molecular dynamics simulations (*30*). The disordered phase persists to the highest stresses measured, indicating that a significant kinetic barrier hinders transformation of α-quartz to stishovite on shock wave time scales. Regardless of the detailed structure of the high-pressure phase, on release, the Hugoniot phase is not quenchable. From the present data, it appears that, upon release, the high-pressure phase reverts to the α-quartz structure in combination with amorphization.

## MATERIALS AND METHODS

Time-resolved XRD measurements coupled with gas-gun–based dynamic compression were carried out at the DCS located at the Advanced Photon Source (APS), Argonne National Laboratory. The DCS allows for the determination of the phase(s) formed under ~100-ns time scale shock loading (*44*). Starting materials consisted of synthetic single-crystal quartz and natural polycrystalline quartz. The single-crystal samples had Z-cut (001), X-cut (110), and Y-cut (100) orientations. The polycrystalline quartz was Arkansas novaculite, a nearly pure quartz rock. The novaculite was untextured and microcrystalline with low porosity. The measured bulk density of the novaculite was 2.640(5) $g/cm^3$. All samples were characterized at ambient conditions using powder or Laue XRD, longitudinal sound velocity measurements, and Archimedean density determination (table S1). The novaculite samples were also characterized with Raman spectroscopy and scanning electron microscopy. All characterization results for ambient samples were consistent with literature values.

The experiments followed procedures described previously (*19*, *44*). The impact configuration is shown schematically in fig. S4. Quartz samples were cut and polished to a thickness of 1 to 2 mm and parallelism of better than 1 mrad. For most experiments, the quartz sample was backed by a [100]-oriented single-crystal LiF window. Two experiments were also performed with no window. Targets were impacted with a 10-mm-diameter [100]-oriented LiF single crystal mounted in a polycarbonate projectile. Projectiles were launched using a two-stage light-gas gun located at the DCS. Projectile velocities ranged from 3.7 to 5.7 km/s, as determined using a measurement system based on four optical beams passing through holes near the muzzle end of the gun barrel. The distance between the beams was calibrated. As the projectile passed each beam, a signal change was recorded on a fast photodiode, allowing the projectile velocity to be determined with a precision of better than 0.5%. For experiments on single-crystal quartz, photon Doppler velocimetry (PDV) was also used to record the projectile velocity history until impact (*45*). Velocities measured with PDV were consistent with those recorded using the optical beam interrupts. Quartz impact stresses were calculated using impedance matching and ranged from 31 to 58 GPa (see the Supplementary Materials). For some of the experiments, an elastic shock wave propagates through the quartz followed by a slower phase transformation wave, whereas for other experiments, a single shock wave brings the quartz from the ambient state directly to the peak state (*31*, *46*, *47*). The elastic shock waves have a good impedance match with the LiF windows, resulting in minimal wave reflection. When the phase transformation shock wave propagating through the quartz reflects from the LiF window, a shock wave propagates back into the sample, resulting in a ~15 to 20% stress increase (fig. S1). Experimental parameters for all plate-impact experiments including projectile velocities, quartz type, sample and window thicknesses, and stresses are listed in table S2.

XRD data were collected in a transmission geometry such that the incoming x-ray beam made an angle of 28° with the impact surface (fig. S4A). X-rays from the third harmonic of the 2.7-cm period undulator at the DCS were used. The experiments were performed in the APS 24-bunch mode of operation, which provides x-ray bunches of ~100-ps duration every 153.4 ns. The energy spectrum of the undulator source is peaked near 23 keV and has an asymmetric shape with a bandwidth of ~1 keV (fig. S4B). Each x-ray bunch contains ~$10^9$ photons. The use of hard x-rays with energy greater than 20 keV allowed for the use of millimeter-thick quartz samples in transmission geometry without excessive x-ray absorption geometry. The lower-order x-ray harmonics were filtered using 250-μm-thick Al and

25-μm-thick Ag foils in the incident beam path, and higher x-ray harmonics were removed by reflecting/focusing the x-rays with Kirkpatrick-Baez mirrors. The typical x-ray beam size incident on the sample was ~300 μm horizontal × 800 μm vertical. The incident x-ray beam was centered vertically on the sample but initially offset horizontally on the impact surface such that the x-ray beam sweeps toward the center of the target between frames due to sample translation. The initial offset was selected to maximize the time before edge release waves intersect the direct incident x-ray beam. With the exception of the late-time data shown in Fig. 6, all diffraction data shown and analyzed correspond to the x-rays probing a uniaxially strained state unaffected by longitudinal or edge release waves.

A four-frame x-ray detection system was used to record diffraction patterns. The x-ray detector has a 150-mm-diameter active area and is positioned perpendicular to and nominally at the center of the direct x-ray beam. Before each shot, an XRD image was collected from a thin polycrystalline silicon calibration target. The sample-detector distance and the instrumental resolution function were determined by performing a Rietveld refinement (*48*) of this silicon diffraction pattern (fig. S2). Typical sample-to-detector distances were approximately 140 mm, allowing us to record diffraction up to scattering angles of about 28°.

The detector system at DCS uses a fast phosphor scintillator that converts scattered x-rays to visible light, which is then directed to one of four intensified charge-coupled device cameras, resulting in each XRD frame corresponding to a single ~100-ps XRD snapshot. Because of the finite x-ray phosphor decay time, particularly strong diffraction peaks are sometimes retained as a ghost image in the following diffraction frame. For most experiments, diffraction images from four consecutive x-ray bunches (153.4 ns between bunches) were recorded. X-ray bunches can also be skipped, allowing the late-time released state to be examined.

The experiments were designed such that at least one XRD frame was obtained while the phase transformation shock wave was propagating through the $SiO_2$ but before the phase transformation wave reached the rear quartz surface. These XRD frames correspond to Hugoniot states. For single-crystal quartz samples, the last such XRD frame recorded (corresponding to the most fully shocked material) was analyzed in detail to determine the structure of the shock-compressed quartz on the Hugoniot. For polycrystalline quartz samples, diffraction rings from uncompressed material ahead of the initial shock front overlap with diffraction rings from the shocked material, precluding quantitative analysis of the singly shocked Hugoniot state. Therefore, analysis of polycrystalline samples was restricted to double-shock data collected after the initial phase transformation shock wave reshocks from the LiF window. A similar analysis of the reshocked state was also performed on some of the single-crystal quartz samples. For reshocked states, the latest XRD frame recorded (before arrival of release waves) corresponding to the most fully reshocked material was analyzed in detail to determine the structure of the reshocked quartz.

The x-ray measurement frame times relative to shock wave breakout at the rear surface of the quartz samples were determined using laser interferometry measurements either at the quartz/LiF interface or at the quartz free surface. Both PDV and Velocity Interferometer System for Any Reflector (VISAR) (*49*) probes were used. The LiF windows had a vapor-deposited Al mirror on the side bonded to the quartz sample. Samples without LiF windows had a vapor-deposited Al mirror on the rear surface of the quartz. A VISAR probe was used to record the shock arrival time at the center of the rear surface of the quartz. Two additional PDV probes located at the same radius from the sample center and colinear with the sample center also provided the shock arrival time at the rear of the quartz sample. The recorded VISAR and PDV signals were correlated to the times at which x-rays were incident on the quartz samples. The four XRD frame times relative to shock breakout are listed in table S5.

VISAR measurements also provided particle velocity histories at the quartz/LiF interfaces (fig. S5). The Hugoniot elastic limit (HEL) for Z-cut quartz is ~15 GPa with an elastic wave velocity of 7.52 km/s (*31*, *50*). Because of the relatively high HEL and relatively large elastic shock speed (*31*), an elastic precursor is observed in all recorded wave profiles for the Z-cut quartz plate-impact experiments. For other quartz crystal orientations as well as novaculite, the HEL is lower and the elastic shock velocities are also lower. The reported elastic velocities are 6.15 km/s for polycrystalline quartz (*46*) and 6.01 and 6.20 km/s for X- and Y-cut quartz, respectively (*31*). This results in the elastic precursor being overdriven by the phase transformation wave for some of the higher stress experiments, consistent with previous measurements (*31*).

## SUPPLEMENTARY MATERIALS

Supplementary material for this article is available at http://advances.sciencemag.org/cgi/content/full/6/35/eabb3913/DC1

## REFERENCES AND NOTES


1. P. D. Asimow, Dynamic compression, in *Treatise on Geophysics*, G. Schubert, Ed. (Elsevier, 2015), pp. 393–416.
2. D. Stöffler, F. Langenhorst, Shock metamorphism of quartz in nature and experiment: I. Basic observation and theory. *Meteoritics* **29**, 155–181 (1994).
3. T. G. Sharp, P. S. DeCarli, *Meteorites and the Early Solar System II* (University of Arizona Press, 2015), pp. 653–677.
4. R. Hemley, C. T. Prewitt, K. J. Kingma, High-pressure behavior of silica. *Rev. Mineral.* **29**, 41–81 (1994).
5. R. M. Wentzcovitch, C. da Silva, J. R. Chelikowsky, N. Binggeli, A new phase and pressure induced amorphization in silica. *Phys. Rev. Lett.* **80**, 2149–2152 (1998).
6. D. M. Teter, R. J. Hemley, G. Kresse, J. Hafner, High pressure polymorphism in silica. *Phys. Rev. Lett.* **80**, 2145–2148 (1998).
7. J. Haines, J. M. Léger, F. Gorelli, M. Hanfland, Crystalline post-quartz phase in silica at high pressure. *Phys. Rev. Lett.* **87**, 155503 (2001).
8. L. S. Dubrovinsky, N. A. Dubrovinskaia, V. Prakapenka, F. Seifert, F. Langenhorst, V. Dmitriev, H.-P. Weber, T. Le Bihan, A class of new high-pressure silica polymorphs. *Phys. Earth Planet. In.* **143–144**, 231–240 (2004).
9. Y. Liang, C. R. Miranda, S. Scandolo, Atomistic pathways of the pressure-induced densification of quartz. *Phys. Rev. B* **92**, 134102 (2015).
10. Q. Y. Hu, J.-F. Shu, W. G. Yang, C. Park, M. W. Chen, T. Fujita, H.-K. Mao, H. W. Sheng, Stability limits and transformation pathways of α-quartz under high pressure. *Phys. Rev. B* **95**, 104112 (2017).
11. R. J. Hemley, A. P. Jephcoat, H. K. Mao, L. C. Ming, M. H. Manghnani, Pressure-induced amorphization of crystalline silica. *Nature* **334**, 52–54 (1988).
12. R. G. McQueen, J. N. Fritz, S. P. Marsh, On the equation of state of stishovite. *J. Geophys. Res.* **68**, 2319–2322 (1963).
13. G. A. Lyzenga, T. J. Ahrens, A. C. Mitchell, Shock temperatures of $SiO_2$ and their geophysical implications. *J. Geophys. Res.* **88**, 2431–2444 (1983).
14. J. A. Akins, T. J. Ahrens, Dynamic compression of $SiO_2$: A new interpretation. *Geophys. Res. Lett.* **29**, 31-1–31-4 (2002).
15. S.-N. Luo, T. J. Ahrens, P. D. Asimow, Polymorphism, superheating, and amorphization of silica upon shock wave loading and release. *J. Geophys. Res.* **108**, (2003).
16. F. Langenhorst, A. Deutsch, Shock metamorphism of minerals. *Elements* **8**, 31–36 (2012).
17. S. L. Chaplot, S. K. Sikka, Molecular-dynamics simulation of shock-stress-induced amorphization of α-quartz. *Phys. Rev. B* **61**, 11205–11208 (2000).
18. W. R. Panero, L. R. Benedetti, R. Jeanloz, Equation of state of stishovite and Interpretation of $SiO_2$ shock-compression data. *J. Geophys. Res.* **108**, 2015 (2003).
19. S. J. Tracy, S. J. Turneaure, T. S. Duffy, In situ X-ray diffraction of shock-compressed fused silica. *Phys. Rev. Lett.* **120**, 135702 (2018).

20. A. E. Gleason, C. A. Bolme, H. J. Lee, B. Nagler, E. Galtier, R. G. Kraus, R. Sandberg, W. Yang, F. Langenhorst, W. L. Mao, Time-resolved diffraction of shock-released $SiO_2$ and diaplectic glass formation. *Nat. Commun.* **8**, 1481 (2017).
21. U. Mansfeld, F. Langenhorst, M. Ebert, A. Kowitz, R. T. Schmitt, Microscopic evidence of stishovite generated in low-pressure shock experiments on porous sandstone: Constraints on its genesis. *Meteorit. Planet. Sci.* **52**, 1449–1464 (2017).
22. K. S. Scheidl, A. Kurnosov, D. M. Trots, T. Boffa Ballaran, R. J. Angel, R. Miletich, Extending the single-crystal quartz pressure gauge up to hydrostatic pressure of 19 GPa. *J. Appl. Cryst.* **49**, 2129–2137 (2016).
23. A. J. Gratz, W. J. Nellis, J. M. Christie, W. Brocious, J. Swegle, P. Cordier, Shock metamorphism of quartz with initial temperatures −170 to +1000 °C. *Phys. Chem. Minerals* **19**, 267–288 (1992).
24. Y. Inamura, Y. Katayama, W. Utsumi, K.-i. Funakoshi, Transformations in the intermediate-range structure of $SiO_2$ glass under high pressure and temperature. *Phys. Rev. Lett.* **93**, 015501 (2004).
25. T. Sato, N. Funamori, Sixfold-coordinated amorphous polymorph of $SiO_2$ under high pressure. *Phys. Rev. Lett.* **101**, 255502 (2008).
26. C. J. Benmore, E. Soignard, S. A. Amin, M. Guthrie, S. D. Shastri, P. L. Lee, J. L. Yarger, Structural and topological changes in silica glass at pressure. *Phys. Rev. B* **81**, 054105 (2010).
27. C. Prescher, V. B. Prakapenka, J. Stefanski, S. Jahn, L. B. Skinner, Y. Wang, Beyond sixfold coordinated Si in $SiO_2$ glass at ultrahigh pressures. *Proc. Natl. Acad. Sci. U.S.A.* **114**, 10041–10046 (2017).
28. G. Shen, H.-P. Liermann, S. Sinogeikin, W. Yang, X. Hong, C.-S. Yoo, H. Cynn, Distinct thermal behavior of $GeO_2$ glass in tetrahedral, intermediate, and octahedral forms. *Proc. Natl. Acad. Sci. U.S.A.* **104**, 14576–14579 (2007).
29. M. Guerette, M. R. Ackerson, J. Thomas, F. Yuan, E. Bruce Watson, D. Walker, L. Huang, Structure and properties of silica glass densified in cold compression and hot compression. *Sci. Rep.* **5**, 15343 (2015).
30. Y. Shen, S. B. Jester, T. Qi, E. J. Reed, Nanosecond homogeneous nucleation and crystal growth in shock-compressed $SiO_2$. *Nat. Mater.* **15**, 60–65 (2016).
31. J. Wackerle, Shock-wave compression of quartz. *J. Appl. Phys.* **33**, 922–937 (1962).
32. R. F. Trunin, G. V. Simakov, M. A. Podurets, B. N. Moiseyev, L. V. Popov, Dynamic compressibility of quartz and quartzite at high pressure. *Izv. Acad. Sci. USSR Phys. Solid Earth* **1**, 13–20 (1971).
33. D. E. Grady, W. J. Murri, G. R. Fowles, Quartz to stishovite: Wave propagation in the mixed phase region. *J. Geophys. Res.* **79**, 332–338 (1974).
34. S. P. Marsh, *LASL Shock Hugoniot Data* (University of California Press, 1980).
35. D. Andrault, R. J. Angel, J. L. Mosenfelder, T. Le Bihan, Equation of state of stishovite to lower mantle pressures. *Am. Mineral.* **88**, 301–307 (2003).
36. T. Sekine, M. Akaishi, N. Setaka, $Fe_2N$-type $SiO_2$ from shocked quartz. *Geochim. Cosmochim. Acta* **51**, 379–381 (1987).
37. V. P. Prakapenka, G. Shen, L. S. Dubrovinsky, M. L. Rivers, S. R. Sutton, High pressure induced phase transformation of $SiO_2$ and $GeO_2$: Difference and similarity. *J. Phys. Chem. Solid* **65**, 1537–1545 (2004).
38. L. Huang, M. Durandurdu, J. Kieffer, Transformation pathways of silica under high pressure. *Nat. Mater.* **5**, 977–981 (2006).
39. L.-G. Liu, W. A. Bassett, J. Sharry, New high-pressure modifications of $GeO_2$ and $SiO_2$. *J. Geophys. Res.* **83**, 2301–2305 (1978).
40. O. Tschauner, S.-N. Luo, P. D. Asimow, T. J. Ahrens, Recovery of stishovite-structure at ambient conditions out of shock-generated amorphous silica. *Am. Mineral.* **91**, 1857–1862 (2006).
41. H. Sowa, The oxygen packings of low-quartz and $ReO_3$ under high pressure. *Z. Kristallogr.* **184**, 257–268 (1988).
42. N. Binggeli, J. R. Chelikowsky, Structural transformation of quartz at high pressures. *Nature* **353**, 344–346 (1991).
43. V. P. Dmitriev, P. Tolédano, V. I. Torgashev, E. K. H. Salje, Theory of reconstructive phase transitions between $SiO_2$ polymorphs. *Phys. Rev. B* **58**, 11911–11921 (1998).
44. S. J. Turneaure, N. Sinclair, Y. M. Gupta, Real-time examination of atomistic mechanisms during shock-induced structural transformation in silicon. *Phys. Rev. Lett.* **117**, 045502 (2016).
45. O. T. Strand, D. R. Goosman, C. Martinez, T. L. Whitworth, W. W. Kuhlow, Compact system for high-speed velocimetry using heterodyne techniques. *Rev. Sci. Instrum.* **77**, 083108 (2006).
46. T. J. Ahrens, V. G. Gregson Jr., Shock compression of crustal rocks: Data for quartz, calcite, and plagioclase rocks. *J. Geophys. Res.* **69**, 4839–4874 (1964).
47. T. J. Ahrens, T. J. Rosenberg, *Shock Metamorphism of Natural Materials*, F. M. French, N. M. Short, Eds. (Mono Book Corp, Baltimore, 1968), pp. 59–81.
48. L. Lutterotti, R. Vasin, H.-R. Wenk, Rietveld texture analysis from synchrotron diffraction images. I. Calibration and basic analysis. *Powder Diffr.* **29**, 76–84 (2014).
49. L. M. Barker, R. E. Hollenbach, Laser interferometer for measuring high velocities of any reflecting surface. *J. Appl. Phys.* **43**, 4669–4675 (1972).
50. R. Fowles, Dynamic compression of quartz. *J. Geophys. Res.* **72**, 5729–5742 (1967).
51. Q. Liu, X. Zhou, X. Zeng, S. N. Luo, Sound velocity, equation of state, temperature and melting of LiF single crystals under shock compression. *J. Appl. Phys.* **117**, 045901 (2015).
52. T. J. Ahrens, M. L. Johnson, Shock wave data for minerals, in *Mineral Physics & Crystallography: A Handbook of Physical Constants*, T. J. Ahrens, Ed. (American Geophysical Union, 1995), pp. 143–184.
53. T. J. Ahrens, G. E. Duvall, Stress relaxation behind elastic shock waves in rocks. *J. Geophys. Res.* **71**, 4349–4360 (1966).
54. M. A. Podurets, G. V. Simakov, G. S. Telegin, On the phase equilibrium in shock-compressed quartz and on the kinetics of phase transitions. *Izv. Earth Phys.* **7**, 3–11 (1976).
55. M. D. Knudson, M. P. Desjarlais, Adiabatic release measurements in α-quartz between 300 and 1200 GPa: Characterization of α-quartz as a shock standard in the multimegabar regime. *Phys. Rev. B* **88**, 184107 (2013).
56. A. P. Hammersley, S. O. Svensson, M. Hanfland, A. N. Fitch, D. Hausermann, Two-dimensional detector software: From real detector to idealised image or two-theta scan. *High Press. Res.* **14**, 235–248 (1996).
57. R. A. Fischer, A. J. Campbell, B. A. Chidester, D. M. Reaman, E. C. Thompson, J. S. Pigott, V. B. Prakapenka, J. S. Smith, Equations of state and phase boundary for stishovite and $CaCl_2$-type $SiO_2$. *Am. Mineral.* **103**, 792–802 (2018).
58. R. Martoňák, D. Donadio, A. R. Oganov, M. Parrinello, Crystal structure transformations in $SiO_2$ from classical and *ab initio* metadynamics. *Nat. Mater.* **5**, 623–626 (2006).


**Acknowledgments:** We thank J. Klug, Y. Li, D. Rickerson, A. Schuman, N. Sinclair, P. Rigg, and B. Williams of the Dynamic Compression Sector for assistance with the impact experiments. B. Glam and D. Kim provided experimental assistance. K. Swadba assisted in the analysis of wave profile data. Y. Gupta is thanked for providing comments after a careful reading of the manuscript. The Arkansas novaculite samples were obtained from the Princeton Mineral Collection. **Funding:** This research was supported by the Defense Threat Reduction Agency (HDTRA1-15-1-0048) and the NSF (EAR-1644614). Washington State University (WSU) provided experimental support through the U.S. Department of Energy (DOE)/National Nuclear Security Agency (NNSA) Award nos. DE-NA0002007 and DE-NA0003957. This work is based on experiments performed at the Dynamic Compression Sector, operated by WSU under DOE/NNSA Award no. DE-NA0002442. This research used the resources of the Advanced Photon Source, a Department of Energy Office of Science User Facility operated for the DOE Office of Science by the Argonne National Laboratory under contract no. DE-AC02-06CH11357. **Author contributions:** S.J.Tr. and S.J.Tu. were responsible for the design and execution of the experiments. All authors carried out the experiments and were involved in discussions related to experimental design and data analysis. All authors contributed to the writing of the manuscript. **Competing interests:** The authors declare that they have no competing interests. **Data and materials availability:** All data needed to evaluate the conclusions in the paper are present in the paper and/or the Supplementary Materials. Additional data related to this paper may be requested from the authors.

Submitted 26 February 2020
Accepted 14 July 2020
Published 26 August 2020
10.1126/sciadv.abb3913

**Citation:** S. J. Tracy, S. J. Turneaure, T. S. Duffy, Structural response of α-quartz under plate-impact shock compression. *Sci. Adv.* **6**, eabb3913 (2020).

Science Advances

# Structural response of α-quartz under plate-impact shock compression

Sally June Tracy, Stefan J. Turneaure and Thomas S. Duffy

*Sci Adv* **6** (35), eabb3913.
DOI: 10.1126/sciadv.abb3913



*Science Advances* (ISSN 2375-2548) is published by the American Association for the Advancement of Science, 1200 New York Avenue NW, Washington, DC 20005. The title *Science Advances* is a registered trademark of AAAS.